



# Transport properties of 3D printed polymer nanocomposites for potential thermoelectric applications

Z. Viskadourakis<sup>1</sup> · G. Perrakis<sup>1,2</sup> · E. Symeou<sup>3</sup> · J. Giapintzakis<sup>3</sup> · G. Kenanakis<sup>1</sup>

Received: 6 December 2018 / Accepted: 31 January 2019  
© Springer-Verlag GmbH Germany, part of Springer Nature 2019

## Abstract

We report the transport and thermoelectric properties of three-dimensional printed samples, which are composed by polymer nanocomposites. For the purposes of the current study, the well-known fused deposition modeling three-dimensional printing method was employed. Commercially available PLA-based nanocomposite filaments, such as PLA–graphite and PLA–graphene, are used to produce mm-scale samples. Electrical conductivity and Seebeck coefficient were investigated, as a function of temperature. PLA–graphene samples exhibit effective thermoelectric performance, comparable to the other state-of-the-art polymer nanocomposites, indicating that commercial polymer nanocomposites can be promising candidates for 3D printed thermoelectric devices.

## 1 Introduction

Thermoelectric (TE) materials have attracted a lot of interest, since they can directly convert heat to electricity through Seebeck effect. Such TE devices possess significant advantages, since they do not pollute, they do not have moving parts, and thus, they do not produce vibrations, and they have already been widely used in waste heat recovery as well as in solid-state cooling [1–5].

The efficiency of a thermoelectric material is determined through the dimensionless thermoelectric figure of merit  $ZT = \sigma \times S^2 \times T / \kappa$ , where  $\sigma$  is the electrical conductivity,  $S$  is the Seebeck coefficient,  $\kappa$  is the thermal conductivity, and  $T$  is the absolute temperature. Hence, an efficient thermoelectric material should exhibit high  $ZT$  values, i.e., high electrical conductivity and Seebeck coefficient along with low thermal conductivity. For thermoelectric applications,  $ZT > 1$  is required. Furthermore, the  $P = \sigma \times S^2$  is known as

thermoelectric power factor and determines the ability of a TE material to convert heat to electricity.

Today, the commercial TE devices are based on inorganic chalcogenides such as BiTe, SbTe, and BiSe alloys [6–12], skutterodites, and transition metal oxides [13]. Thermoelectric performance of such devices is significant, although the TE materials used are expensive and difficult to be produced. Especially, for the chalcogenides, Te is very toxic and rear, they cannot be used in corrosive and highly oxidizing environments, since they are easily oxidized, and chemically metastable. In this regard, it is important to seek for new types of materials which can be produced through simple routes, they will be cost-effective and environmental friendly.

To this point of view, polymer nanocomposites could exploit the next generation of thermoelectric materials because of their low-cost production, their light weight, their easy processability, and their environmental friendly nature. Usually, state-of-the-art polymer composites consist of a conjugated polymer matrix such as polyaniline (PANI) and poly(3,4-ethylenedioxythiophene) poly(styrenesulfonate) (PEDOT:PSS), and a conductive nanofiller, which can be inorganic (such as PbTe, MoS<sub>2</sub>, Te, etc.) [14–16] or carbon nanostructures such as carbon nanotubes, fullerenes, graphene, and graphite [17–21]. The nanofiller introduction results in the fine-tuning of the transport properties, i.e.,  $S$  and  $\sigma$ , towards the enhancement of the TE performance of the polymer composite.

✉ Z. Viskadourakis  
zach@iesl.forth.gr

<sup>1</sup> Institute of Electronic Structure and Laser, Foundation for Research and Technology-Hellas, N. Plastira 100, 70013 Heraklion, Crete, Greece

<sup>2</sup> Department of Materials Science and Technology, University of Crete, 71003 Heraklion, Crete, Greece

<sup>3</sup> Department of Mechanical and Manufacturing Engineering, University of Cyprus, 75 Kallipoleos Avenue, P.O. Box 20537, 1678 Nicosia, Cyprus

Another advantage that polymer nanocomposites exhibit, in comparison to the other inorganic materials, is that many of them can be relatively easily used to produce three-dimensional (3D) printed structures. In general, 3D printing technology has gained exploding attention recently, since it can be used to construct low-cost complex structures. Various methods of 3D printing have been developed, such as stereolithography (SLA), selective laser sintering (SLS) digital light processing (DLP), binder printing, inkjet printing, laminate object manufacturing, etc. [22–24]. Among them, however, the fused deposition modeling (FDM) is an effective 3D printing method using thermoplastic materials (in the form of long wires, called filaments), which are heated above their melting point, while they are pushed through a narrow nozzle. This nozzle is computer-controlled, as well as it moves along all *xyz* directions. Nozzle movements are determined through computer-assisted design (CAD) files; thus, by designing the appropriate structure in a CAD program, nozzle starts to draw the desired pattern, layer by layer, by extruding the molten thermoplastic, and the final structure is build up in such way. FDM process is advantageous, since it is a relatively quick process, while high precision can be achieved, i.e., the resolution of a moderate commercial 3D FDM printer is 50–100  $\mu\text{m}$ , depending on the chosen filament. Considering the above, the idea of printing thermoelectric devices using FDM becomes interesting.

Among other polymers, polylactic acid (PLA) is widely used in FDM printing, due to its effective mechanical, chemical, and thermal properties [25, 26]. Furthermore, polymer nanocomposites with PLA polymer matrix have been produced, which exhibit remarkably promising transport and TE properties [27, 28]. On the other hand, there are PLA-based filaments, already commercially available, which possess good electrical conductivity at room temperature and could be possible candidates for developing TE devices, employing the FDM method. Therefore, it is prudent to investigate them, regarding their TE behavior, i.e., to study the electrical conductivity and Seebeck coefficient of samples, which they have been produced by the FDM process, using such commercially available nanocomposite filaments.

To this point of view, we report the electrical conductivity and Seebeck coefficient of PLA-based polymer nanocomposite samples, which have been produced, using FDM 3D printer. Two different PLA-based filaments were used, i.e., the first includes graphite, while the other includes graphene nanofillers. Both of them are commercially available as conductive PLA filaments, suitable for printing electronic circuits. Extensive characterization regarding their structural, thermal, transport, and thermoelectric properties has been performed. Furthermore, the influence of the FDM process itself is investigated, with respect to the above-mentioned properties. Experimental evidence shows that the studied 3D printed samples and

the corresponding filaments exhibit interesting transport and thermoelectric features, which are related to the thermal behavior of the polymer matrix of the nanocomposites. Furthermore, low Seebeck coefficient in combination with relatively low electrical conductivity results in the reduced thermoelectric performance of both nanocomposites. Moreover, FDM process seems to slightly suppress the overall performance of the nanocomposites.

## 2 Experimental details

### 2.1 Sample preparation

Commercially purchased, PLA-based filaments, compatible with FDM 3D printers, were chosen for this study. In particular, PLA–graphite (Proto-Pasta by ProtoPlant) and PLA–graphene (by BlackMagic3D) nanocomposites are investigated. All the investigated nanocomposites, are conductive; thus, they can be subjected to standard electrical characterization, as described in next sections. From each filament, a cylindrical part has been extracted and studied regarding its structural, thermal, transport, and thermoelectric properties. Furthermore, each filament has been used to produce 3D printed samples. In particular, a dual-extrusion FDM-type 3D printer (Makerbot Replicator 2X) was used for the direct fabrication of 3D printed parallelepiped (approx. 10 mm  $\times$  4 mm  $\times$  0.5 mm) samples. As described in the introduction, in the FMD 3D printing process, the used filament is heated above its melting point and pushed through a moving nozzle. As the nozzle moves in all *xyz* directions, a 3D object is formatted on a surface. In our case, the nozzle has a diameter of 0.6 mm; the filament is heated at 240  $^{\circ}\text{C}$ , while the surface, in which the object is formatted, is kept at 100  $^{\circ}\text{C}$ . 3D printing parameters, such as nozzle speed, extrusion velocity, layer thickness, etc., have been optimized in each case, so as all the produced samples are uniformly printed. Furthermore, for all 3D printed samples, the same printing path is kept, while the 3D printing filling ratio was 100%, and thus, all samples were fully packed.

### 2.2 Characterization

#### 2.2.1 X-ray diffraction experiments

The crystal structures of all the samples were determined by X-ray diffraction (XRD) experiments, using a Rigaku (RINT 2000) diffractometer with Cu  $K\alpha$  ( $\lambda = 1.5406 \text{ \AA}$ ) X-rays for  $2\theta = 10^{\circ}$ – $60^{\circ}$ , and a step time of  $60^{\circ}/\text{s}$ , employing the Bragg–Bretano geometry.

## 2.2.2 Thermal properties experiments

Differential scanning calorimetry (DSC) experiments were performed using a Perkin Elmer Diamond differential scanning calorimeter, in the temperature range 20–180 °C, with a temperature ramp rate of 10 K/min, in both warming and cooling ramps. Furthermore, thermogravimetric analysis (TGA) experiments were performed, using a Perkin Elmer Pyris Diamond TGA unit, for all the samples. The purpose of the latter experiments is to confirm the % w/w loading of the nanofiller into the nanocomposite, given by filament manufacturers. Thus, the temperature during the TGA experiments was increased up to 600 °C, to decompose the PLA without affecting the nanofiller nature. Temperature ramp rate was kept at 10 K/min, while the whole process was done in the air.

## 2.2.3 FT-IR spectroscopy

FT-IR (absorbance) experiments were carried out with a Bruker Vertex 70v FT-IR vacuum spectrometer equipped with a A225/Q Platinum ATR unit with single reflection diamond crystal which allows the infrared analysis of unevenly shaped solid samples and liquids through total reflection measurements, in a spectral range of 3500–500  $\text{cm}^{-1}$ . A broadband KBr detector and a room-temperature broadband triglycine sulfate (DTGS) detector were used, while interferograms were collected at 4  $\text{cm}^{-1}$  resolution (8 scans), apodized with a Blackman–Harris function, and Fourier transformed with two levels of zero filling to yield spectra encoded at 2  $\text{cm}^{-1}$  intervals. Before scanning the samples, a background diamond crystal was recorded, and each sample spectrum was obtained by automatic subtraction of it.

## 2.2.4 DC electrical conductivity

Four-probe resistivity measurements were performed in all the samples (see drawing in Fig. 5). Metallic contacts were being developed on the samples, using conducting silver paste. Copper wires were attached on the silver paste contacts, the other end of which were connected on a Keithley 2400 Source Measure Unit (SMU). Constant current is induced through the sample and the voltage across the leads is measured, so as the resistance  $R$  of the sample is calculated using the Ohm's law, i.e.,  $R = V/I$ . Then, the electrical conductivity  $\sigma$  is extracted using the formula  $\sigma = R L / wt$ , where  $L$  is the distance between the voltage contacts, and  $w$  and  $t$  is the width and the thickness of the sample, respectively. Electrical conductivity has been measured for all the samples in a temperature range from room temperature, up to 180 °C.

## 2.2.5 Seebeck coefficient

Seebeck coefficient measurements were performed for all samples, employing the standard steady-state technique (see drawing in Fig. 6). According to this technique, the sample is attached on a rigid surface, with constant temperature. A heater is also attached on the other end of the sample and it is supplied with a current, causing its heating due to joule effect. The upper end of the sample is heated, and a heat flow is established towards the cold end of the sample. After some time, this heat flow becomes constant, and thus, the temperature difference between the two ends of the sample is constant. This temperature gradient  $\Delta T$  can be measured using two type-E thermocouples. Nevertheless, such gradient produces a voltage drop  $\Delta V$  across the samples, which is also measured using a sensitive voltmeter. Consequently, the Seebeck coefficient  $S_x$  of the sample can be defined as  $S_x = S_{\text{ref}} - \Delta V / \Delta T$ , where  $S_{\text{ref}}$  is the absolute Seebeck coefficient value of the leads, which are used for the measurement of the voltage drop.

It must be noted that the Seebeck coefficient sign is characteristic for the majority of the charge carriers in the sample, i.e., negative  $S_x$  means that electrons dominate the system, while positive  $S_x$  indicates the existence of holes into the system. Seebeck coefficient is also measured in the temperature range up to 180 °C.

## 3 Results and discussion

Figure 1 depicts typical XRD patterns for all the investigated samples. For PLA–graphite samples (black curve), only PLA diffraction peaks are observed [29, 30], while there is not

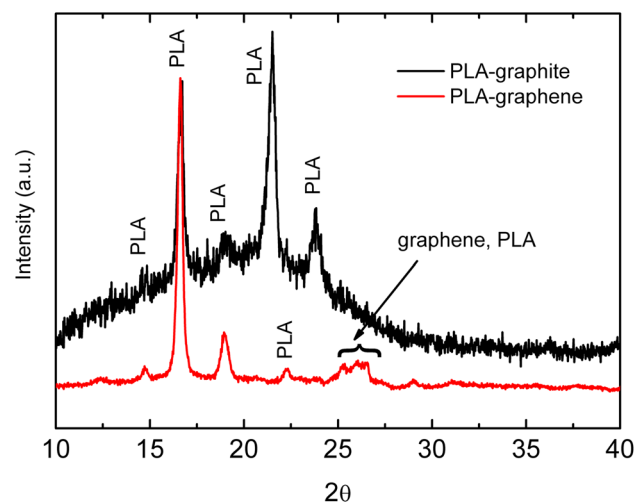


**Fig. 1** XRD pattern for PLA–graphite (black curve) and PLA–graphene (red curve), 3D printed samples. All peaks are assigned according to the literature

any peak observed for graphite [31–33] (main diffraction peak of graphite appears at  $2\theta \sim 27^\circ$ ). On the other hand, PLA–graphene samples (red curve) exhibit a broad shoulder at  $2\theta \sim 27^\circ$  [33–35], which can be indexed to graphene honeycomb structure. Nevertheless, although the large nanofiller was loading for both polymer nanocomposites, nanofiller structure cannot be evidently shown by XRD spectra. In contrast, the semi-crystalline nature of the PLA matrix is clearly observed in all samples, either in filaments, or in 3D-printed samples.

Figure 2 shows the FT-IR spectra for both PLA–graphite (Fig. 2b) and PLA–graphene (Fig. 2c) samples. Pure PLA spectrum is also shown for comparison (Fig. 2a). All the peaks (Table 1) presented here are consistently assigned to the peaks of interest from PLA matrix [36–38]. Interestingly, there are peaks, such as at  $1011\text{ cm}^{-1}$ , which appear on both the PLA–graphite and PLA–graphene samples, while they do not appear to the pure PLA. This could correspond to distinct C–O stretching vibrations, involving the formation of metal nanoparticles by binding C–O with different metal ions [39], although further investigation is needed to

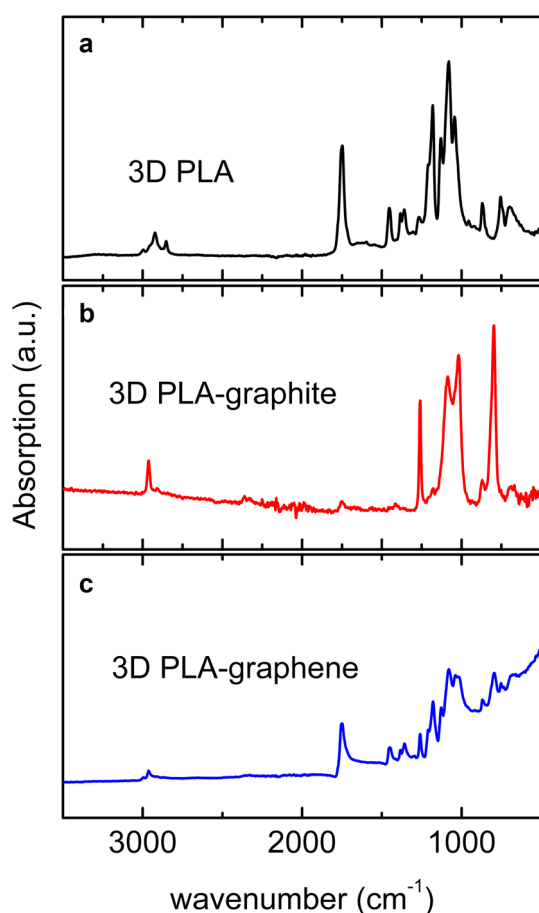


**Fig. 2** FT-IR spectra for **a** pure PLA, **b** PLA–graphite, and **c** PLA–graphene 3D printed samples

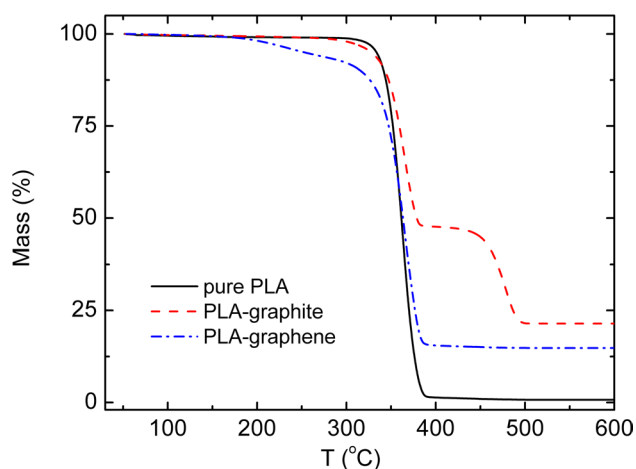
evidently prove such a scenario, which is out of the scope, of the current study. Moreover, there are peaks appeared to pure PLA and they do not appear to neither of the two PLA-based nanocomposites (i.e., peak at  $751\text{ cm}^{-1}$ ), or they appear to one of the two nanocomposites (i.e.,  $698\text{ cm}^{-1}$ ,  $1042\text{ cm}^{-1}$ , etc.). Extensive investigation is needed, to clarify such changes; however, it is out of the scope of this study.

TGA analysis, of all the investigated samples, is shown in Fig. 3. TGA curve for pure PLA (black solid line, Fig. 3) is also shown for comparison. The steep 100% mass reduction in the range  $300\text{--}400^\circ\text{C}$  corresponds to the oxidative decomposition of the PLA, consistently to the previous TGA reports [40, 41]. TGA curve for PLA–graphite (red dashed line, Fig. 3) shows two distinctive degradations. The first one occurs in the temperature range approx.  $300\text{--}400^\circ\text{C}$ , which is due to the decomposition of the PLA, while another one occurs in the range approx.  $400\text{--}500^\circ\text{C}$ . The total weight loss is found to be 79%. Considering that graphite does not exhibit any phase change at this temperature range, it can be concluded that the remaining % weight is due to the graphite, and thus, the investigated PLA–graphite nanocomposite includes graphite fillers as high as 21% w/w. The existence of the second degradation stage ( $400\text{--}500^\circ\text{C}$ ) implies that the other polymer compounds are included to the filament, which they are also decomposed. Here, it must be noted that, according to the filament manufacturer, plasticizer and coupling agent are used in the filament production. Both of them are polymeric compounds. The coupling agent not only contributes to the homogeneous dispersion of the nanofiller, but also improves the polymer/nanofiller interface, resulting in the optimization of the nanocomposite's properties [42–44]. Furthermore, the other plasticizers are included into nanocomposite filaments to optimize their mechanical (and other) properties [45, 46], so as to be suitable for FDM 3D printing. Although there is not any detailed information about, it could be plausibly presumed that PLA compatible plasticizer and coupling agent have been used to produce the PLA–graphite nanocomposite filament used in this study, the decomposition of which is demonstrated through the second degradation, in the TGA curve.

For PLA–graphene sample (Fig. 3, red dashed-dot line), the total mass loss is 85%, and thus, the %w/w concentration of the graphene is 15%, consistently to the manufacturer's specs. Interestingly, another transition is seen in the range  $\sim 150\text{--}270^\circ\text{C}$ , prior to the PLA decomposition transition. This transition cannot be plausibly interpreted. Such feature could be attributed to a possible graphene oxide decomposition [47–49], or to the existence of some kind of plasticizers, used during the production of the filament. On the other hand, similar TGA curve has been obtained for both polystyrene (PS)/graphene nanoplatelets (GNPs) and PS/carbon nanotube composites [50, 51]. In such cases, polymer molecules are attached to the graphene nanoplatelet, due

**Table 1** FT-IR peak position and corresponding assignments for pure PLA, PLA-graphite, and PLA graphene 3D printed samples

Peak position (cm <sup>-1</sup> ) PLA	Peak position (cm <sup>-1</sup> ) PLA-graphite	Peak position (cm <sup>-1</sup> ) PLA-graphene	Assignment according to Refs. [37–40]
698	–	698	C–O–C deformation vibration
751	–	–	C=O stretching
877	877	877	C–COO vibration
–	1011	1011	C–O
1042	–	1042	C–CH <sub>3</sub> stretching
1080	1080	1080	CH <sub>3</sub> deformation C–O–C stretching
1133	–	1133	CH <sub>3</sub> rocking vibration
1177	1177	1177	C–O–C symmetric stretching
1220	–	1220	Phenolic C–OH stretching
1268	1268	1268	C–H bending C–O–C stretching
1355	–	1355	C–H symmetric bending
1382	–	1382	C–H symmetric bending
1453	–	1453	CH <sub>3</sub> asymmetric bending
1748	1748	1748	C=O stretching
2854	2854	2854	CH <sub>3</sub> symmetric and asymmetric stretching vibrations
2924	2924	2924	
2994	2994	2994	

**Fig. 3** Thermogravimetric analysis curves for all the samples: pure PLA, (black curve); PLA-graphite (red dashed line); PLA-graphene (blue dashed-dot line) 3D printed samples

to milling, resulting in a functionalized graphene polymer. Nonetheless, in our case, we cannot clarify the exact origin of this low-temperature degradation, in the TGA curve of the PLA-graphene. Finally, it must be noted that similar TGA curves are obtained for both spool materials and 3D-printed samples, indicating that the FDM process does not affect neither the composition nor the thermal behavior of the nanocomposites.

DSC results, for both spool and 3D printed samples, are demonstrated in Fig. 4. In particular, panels a and b, in Fig. 4 show the temperature dependence of the heat flow, for the pure PLA. Features, typical for semi-crystalline polymers, such as PLA are observed, i.e., an endotherm maximum at 62 °C, which corresponds to the PLA glass transition temperature ( $T_g$ ), a broad exotherm minimum at 118 °C, related to the cold crystallization temperature  $T_c$ , and a sharp endotherm at 150 °C, associated with the melting point,  $T_m$  of the material. It has to be noticed that all the above-mentioned features were observed in DSC curve, during heating. Corresponding cooling curves show an endotherm peak at the 60 °C, thus, at  $T_g$ . Different  $T_g$  values between heating and cooling are resulted most likely due to the experimental artifacts, rather than reflecting a physical explanation. In both cases, the observed  $T_g$  values are similar to values previously reported [38, 52, 53]. A closer inspection PLA DSC heating curve (especially to that of 3D printed sample) reveals two more features; first, there is an endotherm peak at 65 °C, and another short endotherm peak at ~160 °C. The existence of a double endotherm melting, along with the double glass endotherm, suggests the existence of multiple crystalline states, which most likely are formatted during thermal cycling [54]. Thus, PLA is probably affected by the FDM process in which it is heated above its melting point, to be printed, and then, it is cooled down again. Nonetheless, there are not any noticeable differences between spool and 3D-printed samples.



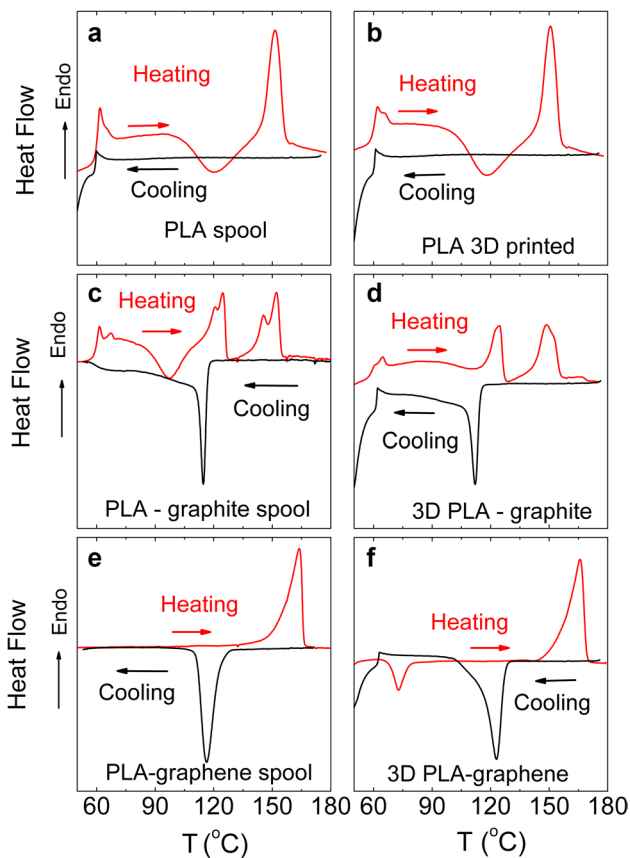


**Fig. 4** Differential scanning calorimetry curves for **a** spool PLA, **b** 3D-printed PLA, **c** spool PLA-graphite, **d** 3D-printed PLA-graphite, **e** spool PLA-graphene, and **f** PLA-graphene 3D printed samples. Heat flow as a function of temperature, upon heating (red solid lines) and cooling (black solid lines), is obtained for all samples

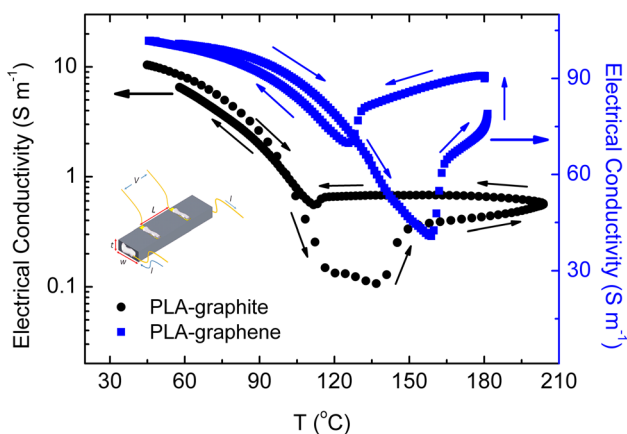


**Fig. 5** Electrical conductivity with respect of the temperature for **a** PLA-graphite (black circles) and **b** PLA-graphene (blue rectangles) 3D printed samples. Black and blue arrows show the evolution of the conductivity, upon heating and cooling. The experimental technique, used for the electrical conductivity measurement, is shown in the drawing included

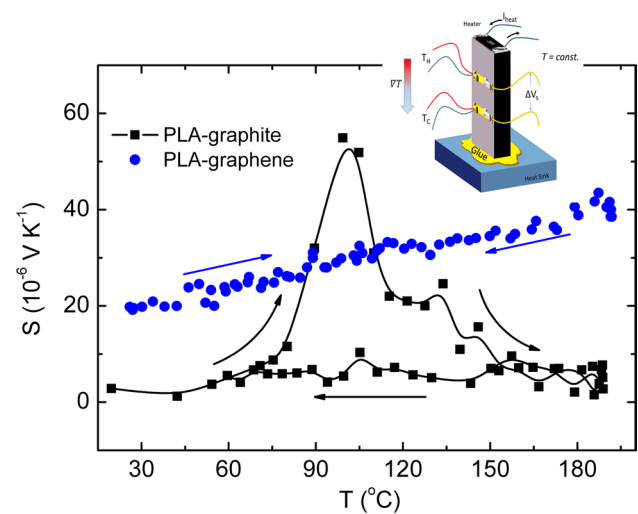
PLA-graphite DSC curves are shown in Fig. 4c, e (raw and 3D-printed samples, respectively). Both heating curves distinctly exhibit two double endotherms at 122–125 °C and 149–152 °C, respectively. The latter obviously corresponds to the melting point of the PLA. The former melting point could be possibly attributed to the dispersants and plasticizers, used during filament production. However, further experiments are needed to clarify this. Furthermore, cooling curve shows a sharp exotherm at 112 °C, suggestive for a fast cold crystallization process taking place at such temperature. The fact that such exotherm is observed only at cooling curve is notable; however, it has been reported for the other polymer composites, containing various carbon structures [55–59]. Comparing DSC curves, between spool and 3D-printed samples, several differences come out. Double endotherms as well as the double peak at  $T_g$  are more pronounced for raw material. Furthermore, during cooling process, 3D-printed sample curve shows endotherm at  $T_g$ , whereas nothing is observed for the spool material. The above-mentioned differences clearly indicate that PLA-graphite raw material is less uniform than the 3D-printed one. For pure PLA, multiple crystalline states have been identified, which are most likely formatted due to thermal cycling. This is probably the case for PLA-graphite, as well. Thermal cycling seems to affect the crystallinity of the PLA-graphite nanocomposite, towards a single uniform state.

Figure 4e, f shows both the heating and cooling the DSC curves, for the PLA-graphene samples (spool and 3D-printed, respectively). During heating, an exotherm is seen at 72 °C and a broad endotherm is observed at 165 °C, for the 3D-printed sample (no exotherm is shown for the spool material). The latter is indicative for the melting temperature of the polymer composite, while the former probably corresponds to a very-low-cold crystallization temperature. Both the high w/w% nanofiller loading and the high-temperature rate used for the DSC process could possibly result in such low crystallization temperatures [59, 60]. In addition, a sharp exotherm is obtained, for both raw and 3D-printed materials at ~ 120 K, during cooling.

DSC experiments reveal that thermal treatment could possibly induce changes in the crystalline state of the nanocomposites; however, they do not affect overall nature of the nanocomposite, in a significant manner. Furthermore, the investigated materials can potentially be used for 3D printed thermoelectric devices. Consequently, it is useful to concentrate to the thermoelectric performance of the 3D-printed samples. Thus, Fig. 5 shows the temperature dependence of the electrical conductivity, for both 3D-printed samples. PLA-graphene sample shows larger conductivity compared to the PLA-graphite one. Furthermore, both conductivity curves show interesting features. In particular, for PLA-graphite, conductivity decreases up to 120 °C; then, it

remains almost constant up to 145 °C, and then, it increases again up to the highest measured temperature. Both temperatures mentioned above coincide with the corresponding temperatures where endotherms are observed in DSC experiments. Furthermore, during cooling resistivity exhibits a minimum at ~ 110 °C, agreeing with the corresponding exotherm (Fig. 3d). Conductivity features, which are well matched to the DSC results, are also obtained for PLA-graphene samples. Therefore, transport properties are straightly correlated to the thermal properties, indicating that thermal cycling definitely affects the electrical performance of the investigated nanocomposites. Extensive studies regarding the rheological properties of the nanocomposites are needed, to clarify the exact mechanism which correlates their thermal and transport properties. Comparing to other thermoelectric polymer nanocomposites and nanocomposites used in 3D-printing [14, 18–20, 27, 45, 61–63], PLA-graphite cannot be considered as competitive, due to its low conductivity. In contrast, PLA graphene's conductivity is promising, i.e., it is higher than that of acrylonitrile butadiene styrene/zinc oxide (CABS/ZnO) [64], it is comparable to that of PLA/BST [27], but still inferior to the conductivity of PANI/GNs [63], for example.

Seebeck coefficient as a function of temperature is shown in Fig. 6.  $S$  values for PLA-graphite samples (Fig. 6) are very low (i.e., 2–3  $\mu\text{V/K}$ ), although positive, indicating that holes are the dominant charge carriers, into the system. Such  $S$  are lower than others reported for polyaniline (PANI)/graphite oxide nanocomposites [20]; however, they are comparable to those reported CABS/ZnO samples, fabricated by the FDM technique [64]. Although their low values, Seebeck coefficient curve, show distinctive features, similar to the others obtained from the conductivity curve. In particular, upon heating,  $S$  shows an abrupt increment at ~ 115 °C ( $S \sim +70 \mu\text{V/K}$ ), then it decreases down to ~ 20–25  $\mu\text{V/K}$ , up to 150–160 °C, and then it drops down to 2–3  $\mu\text{V/K}$ . Upon cooling,  $S$  remains almost constant, to 2–3  $\mu\text{V/K}$ , while a soft shoulder is observed at ~ 115 °C. These observed temperatures exactly coincide with those in electrical conductivity curves, and, consequently, with endotherms observed on the DCS curves. On the other hand, PLA-graphene samples exhibit higher  $S$  values (Fig. 6). Such  $S$  values are comparable (or sometimes superior) to the other values reported for several nanocomposite-containing graphene nanosheets (GNs) [62, 63, 65]. Furthermore, a linear response of the  $S$  with respect to the temperature is obviously seen, upon both warming and cooling. No peaks or shoulders are observed, which can be related/correlated to the corresponding endotherms obtained from the DSC cures. It seems that the appropriate choice of the nanofiller material could result to the suppression or the elimination of the properties of the polymer matrix, towards the enhancement of the thermoelectric performance of the polymer nanocomposite.



**Fig. 6** Seebeck coefficient as a function of temperature, for PLA-graphite (black rectangulars) and PLA-graphene (blue circles). Arrows show the  $S$  change upon heating and cooling. The black solid line is guide to the eye. The steady-state technique used for the  $S$  measurement is pictured in the included drawing

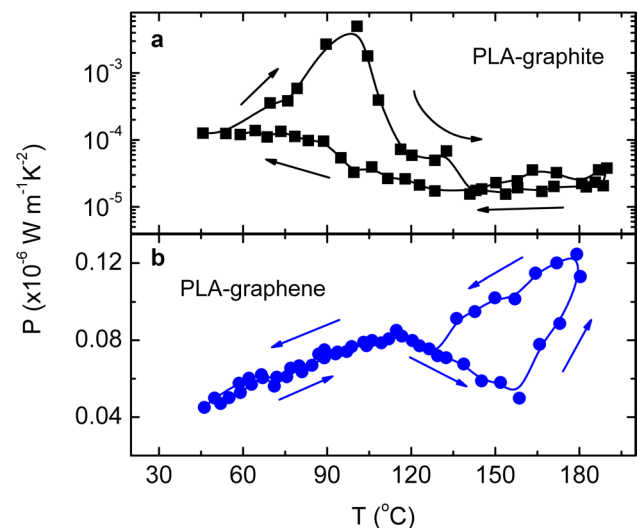


**Fig. 7** Power factor values for **a** PLA-graphite and **b** PLA-graphene. Arrows show the temperature evolution. Black and blue solid lines are guide to the eyes

Power factor  $P$ , as a function of temperature, is demonstrated in Fig. 7. For both 3D-printed samples.  $P$  values obtained for PLA-graphite (Fig. 7a) are extremely low, thus forbidding for potential applications. Low  $P$  values are mainly resulted from the low  $S$  values. Nevertheless,  $P$  curve possesses a local peak at ~ 115 °C, mainly due to the corresponding peak observed in  $S$  curve. However, even in its peak value,  $P$  is almost three orders of magnitude lower than the other polymer nanocomposites, with graphite oxide nanofillers [20]. On the other hand, PLA-graphene 3D samples exhibit much more

improved power factor values, most likely due to both their enhanced Seebeck coefficient and their high electrical conductivity, although the room-temperature  $P$  values obtained are comparable to those reported for PANI/GNs thin films and pellets [62, 63], which are not appropriate for FDM printing yet. Compared to the other nanocomposite filaments, suitable for FDM printing, such as polyetheretherketone (PEEK)/graphene nanoplatelets (GNPs) [5], and CABS/ZnO 3D-printed nanocomposite samples [64], our PLA-graphene sample exhibits significantly improved  $P$  values, indicating that PLA-graphene nanocomposites are promising candidates for 3D printed thermoelectric applications. Furthermore,  $P$  values for PLA-graphene are still lower than those obtained for PLA-Bi<sub>0.5</sub>Sb<sub>0.5</sub>Te (BST) wires, appropriate for FDM printing [27]. However, in the latter case, the produced filaments have not been used to produce 3D printed samples yet.

Regarding the  $ZT$ , we cannot determine it, since thermal conductivity experimental results are required. Notably, measurement of the thermal conductivity of bulk samples, especially in temperatures above room temperature, is a challenging procedure, utilizing complex methods. Regarding the polymer nanocomposites, such as PLA-graphite and PLA-graphene, there are several reports on their thermal conductivity. In general, pure PLA exhibits low thermal conductivity, i.e.,  $\kappa \sim 0.1\text{--}0.2$  W/m/K (room-temperature values) [66, 67]. Carbon inclusions (either graphite or graphene) increase  $\kappa$ , with respect to the kind of the nanofiller, as well as the nanofiller loading [66, 68, 69]. Of course, the above thermal conductivity behavior is considered for PLA-based nanocomposites, which they have not been used for the FDM process. Extensive studies show that 3D printing factors (printing speed, printing patterns, infill, printing orientations, etc.) have a dramatic impact to the thermal conductivity of a 3D printed sample [70–72]. Herein, though we could roughly estimate the  $ZT$ , using  $\kappa$  values, for the corresponding bulk materials, reported in the literature. For the 20% wt. PLA-graphite [67],  $\kappa \sim 3$  W/m/K, which results in a  $ZT \sim 10^{-8}$  at room temperature, which is a considerably low  $ZT$  value. Considering the 15% wt. PLA-graphene [73],  $\kappa \sim 0.8$  W/m/K leading to  $ZT \sim 10^{-5}$ , which is also a very-low room-temperature value. Thus, thermoelectric figure of merit, of the studied PLA nanocomposites, is a real obstacle, regarding their use in potential thermoelectric applications, although improvement of their electrical conductivity and Seebeck coefficient could effectively combine with their low thermal conductivity, towards their use in potential thermoelectric applications.

## 4 Summary and conclusions

In the current study, we investigated the thermoelectric performance of 3D-printed nanocomposite polymeric samples, i.e., PLA-graphite, and PLA-graphene, produced using

appropriate, commercially available filaments, employing the so-called FDM method. Both XRD and FT-IR spectra reveal typical features of the PLA matrix, for both PLA-graphite and PLA-graphene nanocomposites, consistent with the literature. For both nanocomposites, the amount of the nanofiller inclusion is extracted from the TGA curves, which is consistent with the values given by the filament manufacturers. Furthermore, TGA experiments reveal that plasticizers and coupling agents have been used, by the manufacturers, to improve the homogeneous distribution of the nanofillers into the polymer matrix, as well as to enhance their mechanical properties, making them appropriate for FDM printing. Finally, DSC experiments show typical crystallization/recrystallization process for PLA and  $T_g$  values obtained are consistent to the literature.

Electrical conductivity vs. temperature curves, for both nanocomposites, roughly follow the corresponding DSC ones, indicating the effect of the thermal properties to the conduction of the nanocomposites. Thus, it becomes essential to extensively investigate the thermal and rheological properties of both PLA nanocomposites, towards the optimization of their conductivity. PLA-graphene 3D printed samples exhibit an order of magnitude higher electrical conductivity than the PLA-graphite ones. Compared to the other conductive polymer composite materials, PLA-graphene seems to be a promising candidate, while the PLA-graphite has to be improved, regarding its electrical conductivity, to be competitive.

Furthermore, Seebeck coefficient for PLA-graphite is quite low, forbidding for thermoelectric applications. Nevertheless, from both DSC and Seebeck coefficient curves, it is revealed that Seebeck coefficient is directly related to the thermal behavior of the polymer composite. For PLA-graphene,  $S$  exhibits higher values, compared to the PLA-graphite; however, it is still inferior compared to state-of-the-art thermoelectric polymer nanocomposites, such as PLA/BST. Increasing the nanofiller loading, or introducing another type of nanofiller along with the existed, could possibly result in the improvement of the  $S$ , in both cases, although great attention must be paid so as the nanocomposite remains suitable for FDM printing.

As a result, power factor values obtained for PLA-graphite are realistically, not promising for thermoelectric applications. Instead, for PLA-graphene, it shows a better thermoelectric performance, but still lower than the other thermoelectric polymer nanocomposites. In both cases, poor electrical conductivity and relatively low  $S$  values result in such thermoelectric performance.

Despite their substandard thermoelectric performance, both PLA-based nanocomposites exhibit a large advantage, which is that they both can be used in FDM printing. Thus, the optimization of their thermoelectric performance (by increasing the electrical conductivity in combination with



increasing the Seebeck coefficient), along with their superior FDM-compatible properties, would be beneficial, so as both PLA-graphite and PLA-graphene nanocomposites would become state-of-the-art materials for 3D printed thermoelectric devices.

**Acknowledgements** This research has been co-financed by the European Union and Greek national funds through the Operational Program Competitiveness, Entrepreneurship and Innovation, under the call RESEARCH-CREATE-INNOVATE (project code: T1EDK-02784; acronym: POLYSHIELD). Z.V. would like to thank Prof. Theodora Kyratsi (Mechanical and Manufacturing Engineering Department, University of Cyprus), for her limitless help and fruitful discussions.

## References

1. M. Ziabari, D. Zebarjadi, Vashae, A. Shakouri, Rep. Prog. Phys. **79**, 095901 (2016)
2. X. Shi, L. Chen, C. Uher, Int. Mater. Rev. **61**, 379 (2016)
3. K. Koumoto, R. Funahashi, E. Guilmeau, Y. Miyazaki, A. Weidenkaff, Y. Wang, C. Wan, J. Am. Ceram. Soc. **96**, 1 (2013)
4. J.H. Bahk, H. Fang, K. Yazawa, A. Shakouri, J. Mater. Chem. C **3**, 10362 (2015)
5. J. Gonçalves, P. Lima, B. Krause, P. Pötschke, U. Lafont, J. Gomes, C. Abreu, M. Paiva, J. Covas, J. Gonçalves, P. Lima, B. Krause, P. Pötschke, U. Lafont, J.R. Gomes, C.S. Abreu, M.C. Paiva, J.A. Covas, Polymers **10**, 925 (2018)
6. Q. Poudel, Y. Hao, Y. Ma, A. Lan, B. Minnich, X. Yu, D. Yan, A. Wang, D. Muto, X. Vashae, J. Chen, M.S. Liu, G. Dresselhaus, Chen, Z. Ren, Science **320**, 634 (2008)
7. T.P. Hogan, A. Downey, J. Short, J. D'Angelo, C.I. Wu, E. Quarez, J. Androulakis, P.F.P. Poudeu, J.R. Sootsman, D.Y. Chung, M.G. Kanatzidis, S.D. Mahanti, E.J. Timm, H. Schock, F. Ren, J. Johnson, E.D. Case, J. Electron. Mater. **36**, 704 (2007)
8. Y. He, T. Zhang, X. Shi, S.H. Wei, L. Chen, NPG Asia Mater. **7**, 210 (2015)
9. P.F.P. Poudeu, A. Guéguen, C.I. Wu, T. Hogan, M.G. Kanatzidis, Chem. Mater. **22**, 1046 (2010)
10. D.K. Bhat, S.U. Shenoy, J. Phys. Chem. C **121**, 7123 (2017)
11. H.Q. Yang, L. Miao, C.Y. Liu, C. Li, S. Honda, Y. Iwamoto, R. Huang, S. Tanemura, ACS Appl. Mater. Interfaces **7**, 14263 (2015)
12. Z. Li, N. Miao, J. Zhou, Z. Sun, Z. Liu, H. Xu, Nano Energy **43**, 285 (2018)
13. J.E. Rodríguez, L.C. Moreno, Mater. Lett. **65**, 46 (2011)
14. Y. Wang, K. Cai, X. Yao, ACS Appl. Mater. Interfaces **3**, 1163 (2011)
15. L. Wang, J. Schindler, J.A. Thomas, C.R. Kannewurf, M.G. Kanatzidis, Chem. Mater. **7**, 1753 (1995)
16. K.C. See, J.P. Feser, C.E. Chen, A. Majumdar, J.J. Urban, R.A. Segalman, Nano Lett. **10**, 4664 (2010)
17. J. Sun, M.L. Yeh, B.J. Jung, B. Zhang, J. Feser, A. Majumdar, H.E. Katz, Macromolecules **43**, 2897 (2010)
18. K. Zhang, M. Davis, J. Qiu, L. Hope-Weeks, S. Wang, Nanotechnology **23**, 385701 (2012)
19. J. Xiang, L.T. Drzal, Polymer (UK) **53**, 4202 (2012)
20. Y. Zhao, G.-S. Tang, Z.-Z. Yu, J.-S. Qi, Carbon N. Y. **50**, 3064 (2012)
21. K. Zhang, Y. Zhang, S. Wang, Sci. Rep. **3**, 3448 (2013)
22. A. Gebhardt, J.-S. Hötter, in *Additive Manufacturing* (Carl Hanser Verlag GmbH & Co. KG, München, 2016). <https://doi.org/10.3139/9781569905838.fm> (ISBN 978-1-4987-1477-8)
23. J.P. Kruth, M.C. Leu, T. Nakagawa, CIRP Ann. **47**, 525 (1998)
24. N. Guo, M.C. Leu, Front. Mech. Eng. **8**, 215 (2013)
25. M. Ajioka, K. Enomoto, K. Suzuki, A. Yamaguchi, J. Environ. Polym. Degrad. **3**, 225 (1995)
26. J. Lunt, Polym. Degrad. Stab. **59**, 145 (1998)
27. J. Wang, H. Li, R. Liu, L. Li, Y.H. Lin, C.W. Nan, Compos. Sci. Technol. **157**, 1 (2018)
28. M.A. Zhang, J. Kandadai, S. Cech, Roth, S.A. Curran, J. Phys. Chem. B **110**, 12910 (2006)
29. F.A. dos Santos, M.I.B. Tavares, Polímeros **24**, 561 (2014)
30. M. Maiza, M.T. Benaniba, G. Quintard, V. Massardier-Nageotte, Polimeros **25**, 581 (2015)
31. V. Kanakaiah, M. Latha, B. Sravan, A. Palanisamy, J.V. Rani, J. Electrochem. Soc. **161**, A1586 (2014)
32. A.K. Mishra, S. Ramaprabhu, AIP Adv. **1**, 032152 (2011)
33. S. Sasi, A. Murali, S.V. Nair, A.S. Nair, K.R.V. Subramanian, J. Mater. Chem. A **3**, 2717 (2015)
34. P. Karthika, Soft Nanosci. Lett. **2**, 59 (2012)
35. F. Akbar, M. Kolahdouz, S. Larimian, B. Radfar, H.H. Radamson, J. Mater. Sci. Mater. Electron. **26**, 4347 (2015)
36. P.N. Khanam, D. Ponnammma, M.A. AL-Madeed, in *Graphene-Based Polymer Nanocomposites in Electronics*, ed. by K. Sadasivuni, D. Ponnammma, J. Kim, S. Thomas (Springer, Cham, 2015). <https://doi.org/10.1007/978-3-319-13875-6> (ISBN 978-3-319-13875-6)
37. S. Doganay, C. Coskun, Kaynak, H.E. Unalan, Compos. Part B Eng. **99**, 288 (2016)
38. M.A. Cuiffo, J. Snyder, A.M. Elliott, N. Romero, S. Kannan, G.P. Halada, Appl. Sci. **7**, 579 (2017)
39. S. Chandra, S. Bag, P. Das, D. Bhattacharya, P. Pramanik, Chem. Phys. Lett. **519**, 59 (2012)
40. J.P. Mofokeng, A.S. Luyt, T. Tábi, J. Kovács, J. Thermoplast. Compos. Mater. **25**, 927 (2012)
41. J. Alam, M. Alam, M. Raja, Z. Abduljaleel, L.A. Dass, Int. J. Mol. Sci. **15**, 19924 (2014)
42. G. Wu, L. Ma, Y. Wang, L. Liu, Y. Huang, Compos. Part A Appl. Sci. Manuf. **84**, 1 (2016)
43. Y. Xie, C.A.S. Hill, Z. Xiao, H. Militz, C. Mai, Compos. Part A Appl. Sci. Manuf. **41**, 806 (2010)
44. S.-H. Su, Y. Huang, S. Qu, W. Liu, R. Liu, L. Li, Diam. Relat. Mater. **81**, 161 (2018)
45. N. Wang, X. Zhang, X. Ma, J. Fang, Polym. Degrad. Stab. **93**, 1044 (2008)
46. M.P. Arrieta, MdelM. Castro-López, E. Rayón, L.F. Barral-Losada, J.M. López-Vilariño, J. López, M.V. González-Rodríguez, J. Agric. Food Chem. **62**, 10170 (2014)
47. A. Hussein, S. Sarkar, B. Kim, J. Mater. Sci. Technol. **32**, 411 (2016)
48. R. Gao, N. Hu, Z. Yang, Q. Zhu, J. Chai, Y. Su, L. Zhang, Y. Zhang, Nanoscale Res. Lett. **8**, 32 (2013)
49. T. Kuila, A.K. Mishra, P. Khanra, N.H. Kim, J.H. Lee, Nanoscale **5**, 52 (2013)
50. H. Wu, W. Zhao, H. Hu, G. Chen, J. Mater. Chem. **21**, 8626 (2011)
51. G. Viswanathan, N. Chakrapani, H. Yang, B. Wei, H. Chung, K. Cho, C.Y. Ryu, P.M. Ajayan, J. Am. Chem. Soc. **125**, 9258 (2003)
52. R.B. Valapa, G. Pugazhenth, V. Katiyar, RSC Adv. **5**, 28410 (2015)
53. X. Cao, A. Mohamed, S.H. Gordon, J.L. Willett, D.J. Sessa, Thermochim. Acta **406**, 115 (2003)
54. A. Jalali, M.A. Huneault, S. Elkoun, J. Mater. Sci. **51**, 7768 (2016)
55. K. Gnanasekaran, T. Heijmans, S. van Bennekom, H. Woldhuis, S. Wijnia, G. de With, H. Friedrich, Appl. Mater. Today **9**, 21 (2017)
56. C. Hu, Z. Li, Y. Wang, J. Gao, K. Dai, G. Zheng, C. Liu, C. Shen, H. Song, Z. Guo, J. Mater. Chem. C **5**, 2318 (2017)
57. P. Manafi, I. Ghasemi, M. Karrabi, H. Azizi, P. Ehsaninamin, Soft Mater. **12**, 433 (2014)

58. H. Yao, Z. Fan, H. Cheng, X. Guan, C. Wang, K. Sun, J. Ouyang, *Macromol. Rapid Commun.* **39**, 1700727 (2018)
59. S. Jia, D. Yu, Y. Zhu, Z. Wang, L. Chen, L. Fu, *Polymers (Basel)*. **9**, 528 (2017)
60. Y. Chen, X. Yao, Q. Gu, Z. Pan, J. Polym. Eng. **26**, 377 (2013)
61. K. Li, S. Cai, Shen, S. Chen, *Synth. Met.* **197**, 58 (2014)
62. Y. Du, S.Z. Shen, W. Yang, R. Donelson, K. Cai, P.S. Casey, *Synth. Met.* **161**, 2688 (2012)
63. Y. Lu, Y. Song, F. Wang, *Mater. Chem. Phys.* **138**, 238 (2013)
64. Y.Y. Aw, C.K. Yeoh, M.A. Idris, P.L. Teh, K.A. Hamzah, S.A. Sazali, *Materials* **11**, 466 (2018)
65. X. Li, L. Liang, M. Yang, G. Chen, C.Y. Guo, *Org. Electron.* **38**, 2000 (2016)
66. O.J. Botlhoko, J. Ramontja, S.S. Ray, *RSC Adv.* **7**, 33751 (2017)
67. M. Karkri, Thermal conductivity of biocomposite materials, in *Biopolymer Composites in Electronics*, ed. by K.K Sadasivuni, J-J. Cabibihan, D. Ponnammma, M.A.S.A Al-Maadeed, J. Kim (Elsevier, Amsterdam, 2016). <https://doi.org/10.1016/B978-0-12-809261-3.00004-8>
68. B. Mortazavi, F. Hassouna, A. Laachachi, A. Rajabpour, S. Ahzi, D. Chapron, V. Toniazio, D. Ruch, *Thermochim. Acta* **552**, 106 (2013)
69. Z. Antar, H. Noel, J.F. Feller, P. Glouannec, K. Elleuch, *Mater. Sci. Forum* **714**, 115 (2012)
70. Y. Han, J. Purdue Undergrad. Res. **6**, 89 (2016)
71. S.F. Costa, F.M. Duarte, J.A. Covas, *Virtual Phys. Prototyp.* **10**, 35 (2015)
72. T.J. Quill, M.K. Smith, T. Zhou, M.G.S. Baioumy, J.P. Berenguer, B.A. Cola, K. Kalaitzidou, T.L. Bougher, *Appl. Compos. Mater.* **25**, 1205 (2018)
73. P. Lamberti, G. Spinelli, P.P. Kuzhir, L. Guadagno, C. Naddeo, V. Romano, R. Kotsilkova, P. Angelova, V. Georgiev, *AIP Conf. Proc.* **1981**, 020158 (2018)

**Publisher's Note** Springer Nature remains neutral with regard to jurisdictional claims in published maps and institutional affiliations.